

Article

Study and Implementation of a Two-Phase Interleaved Bidirectional DC/DC Converter for Vehicle and DC-Microgrid Systems

Ching-Ming Lai ^{1,*}, Yuan-Chih Lin ² and Dasheng Lee ³

¹ Department of Vehicle Engineering, National Taipei University of Technology, 1, Sec. 3, Chung-Hsiao E. Rd., Taipei 106, Taiwan

² AcBel Polytech Inc., New Taipei City 251, Taiwan; E-Mail: gero.lin1980@gmail.com

³ Department of Energy and Refrigerating Air-Conditioning Engineering, National Taipei University of Technology, 1, Sec. 3, Chung-Hsiao E. Rd., Taipei 106, Taiwan; E-Mail: fl1167@ntut.edu.tw

* Author to whom correspondence should be addressed; E-Mail: pecmlai@gmail.com; Tel.: +886-2-2771-2171 (ext. 3612); Fax: +886-2-2731-4990.

Academic Editor: Omar Hegazy

Received: 21 July 2015 / Accepted: 8 September 2015 / Published: 14 September 2015

Abstract: The objective of this paper is to implement a two-phase, interleaved, bidirectional DC/DC converter topology with an improved voltage conversion ratio for electric vehicle (EV) and DC-microgrid systems. In this study, a two-phase interleaved charge-pump topology is introduced to achieve a high voltage conversion ratio with very simple control circuits. In discharge mode, the circuit topology acts as a voltage-multiplier boost converter to achieve a high step-up conversion ratio (48 V to 240 V). In charge mode, the circuit topology acts as a voltage-divider buck converter to achieve a high voltage step-down conversion ratio (240 V to 48 V). The circuit configuration, operating principle, steady-state analysis and the closed-loop control of the proposed converter are presented. Experiments conducted on a laboratory prototype with 500 W power-rating are presented to verify the effectiveness. The maximum efficiency levels in discharge and charge modes are about 97.7% and 98.4% respectively.

Keywords: interleaved bidirectional converter; improved voltage conversion ratio; vehicle and DC-microgrid systems

1. Introduction

In recent years, due to the shortage of fossil fuels and serious environment problems, much effort has been focused on the development of environmentally friendly distributed generation (DG) technologies [1–4]. It is well known that when many DGs are connected to utility grids, they can cause problems, such as voltage rise and protection problems in the utility grid [5–8]. To solve these problems, new concepts of electric power systems are proposed, and DC-microgrid is one of the solutions [9–12]. Figure 1 shows the system structure of DC-microgrid, it includes grid-connected converter (GCC), wind-turbine based generation system, PV generation system, battery energy system (BES), electric vehicle (EV) and local emergency loads. The function of GCC is to keep DC-bus voltage constant. In order to ensure the reliability of operation for a DC-microgrid, a mass of battery energy storage systems usually needs access into the system. The electric vehicle can provide ancillary services for DC-microgrid, called vehicle to DC-microgrid, which makes clean and efficient electric-powered transportation possible by allowing electric vehicles to power and be powered by the grid. In such applications, the bidirectional DC/DC converter plays an important role in system. Briefly speaking, the voltage difference between the electric vehicle battery/BES and the DC-bus is large; thus, a bidirectional DC/DC converter with a high step-up/down voltage conversion ratio is required.

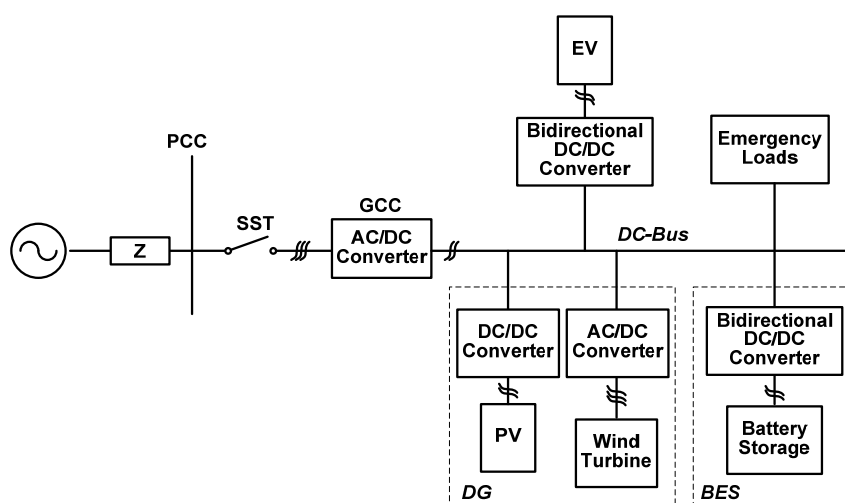


Figure 1. System structure of DC-microgrid.

The conventional buck/boost bidirectional converter has simple circuit structure; however, the voltage conversion ratio is significantly limited because of the effect of parasitic elements [13,14]. In previous studies, the bidirectional converter has been classified into two categories, namely, isolated [15–18] and non-isolated [19–23]. Moreover, the high voltage conversion ratio of bidirectional DC/DC converters is achieved by adjusting the turn ratios of the isolated transformer, such as flyback-type, forward-flyback-type. These converters have a simple and low-cost configuration [15–18]. However, it is only suitable in low-power applications because of its high voltage stress and leakage inductance energy. Additionally, using high-voltage transformers with a large turn-ratio also introduces several problems. For example, the leakage inductance and the parasitic capacitance formed by the secondary winding of the transformer may cause voltage and current spikes and increases loss and noise that will degrade the system performance significantly and damage circuit components.

To overcome the aforementioned drawbacks of the transformer-based converter, the active-clamp technique is introduced to recycle the energy stored in the leakage inductance and absorbs the voltage spikes on the main switch voltage [19,20]. Prior art of a non-isolated bidirectional converter, the three-level bidirectional converter has only half of the voltage stress on the switch compared with conventional bidirectional converters. However, due to the voltage conversion ratio is the same with that of the conventional buck/boost bidirectional converter; thus, the three-level bidirectional converter is not suitable for the large voltage difference between the DC-bus and the battery applications [21]. Compared with isolation transformer based converters, bidirectional converters with coupled-inductors for non-isolation applications possess simpler winding structure and lower conduction loss [22–25]. However, the energy stored in the leakage inductor of the coupled inductor causes a high voltage spike on the power switches. Furthermore, although the extreme duty ratio is avoided, the input current ripple is large due to their single-phase operation, which renders these converters unsuitable for high power and high current applications.

In this paper, a multi-phase interleaved bidirectional converter with an improved voltage conversion ratio for vehicle battery connected to DC-microgrid system applications is presented. A two-phase interleaved charge-pump converter is introduced to achieve a high conversion ratio with very simple control scheme. In discharge mode, the topology acts as a voltage-multiplier boost converter to achieve high step-up conversion. In charge mode, the converter acts as a voltage-divider buck converters to achieve high voltage step-down conversion. Due to the lower duty ratio, not only can the output voltage regulation range be further extended but also the resulting conduction loss can be further reduced due to the shorter conduction period. In addition, the proposed structure benefits reducing voltage stress of the main active switches, which enables one to adopt lower voltage rating devices to further reduce both switching and conduction losses. Accordingly, because of the device voltage stress reduction, high efficiency can be achieved.

2. Circuit Configurations and Operation Principles

Figure 2 shows the circuit topology of the proposed bidirectional converter. The studied structure of two-phase interleaved charge-pump converter is similar to a conventional buck/boost converter except two active high-side switches in series and a charge-pump capacitor employed in the power path. The circuit structure is simple and it can reach an improved voltage conversion ratio with lower duty ratio. Therefore, it can reduce the conduction loss of the switch, to further upgrade the efficiency of the whole bidirectional converter. The proposed converter can transmit energy in both directions. When the energy flows from V_H to V_L , it operates in charge mode (*i.e.*, buck operation); Q_1 and Q_2 are controlled to regulate the output. Thus, Q_1 and Q_2 are defined as the active switches, while Q_3 and Q_4 are the passive switches. The passive switches work as the synchronous rectification. When the energy flows from V_L to V_H , it operates in discharge mode (*i.e.*, boost operation); Q_3 and Q_4 are controlled to regulate the output. Thus, Q_3 and Q_4 are defined as the active switches, while Q_1 and Q_2 are the passive switches. Before the analysis, the following assumptions should be made: (1) the proposed converter is operated in continuous-conduction-mode (CCM); (2) capacitors C_H and C_L is large enough to be considered as a voltage source; (3) the two inductor L_1 and L_2 have the same inductor L_s ; (4) all power semiconductors

are ideal; and (5) the charge-pump voltage V_{CB} is treated as a pure DC and considered as constant, and V_{CB} is equal to $V_H/2$.

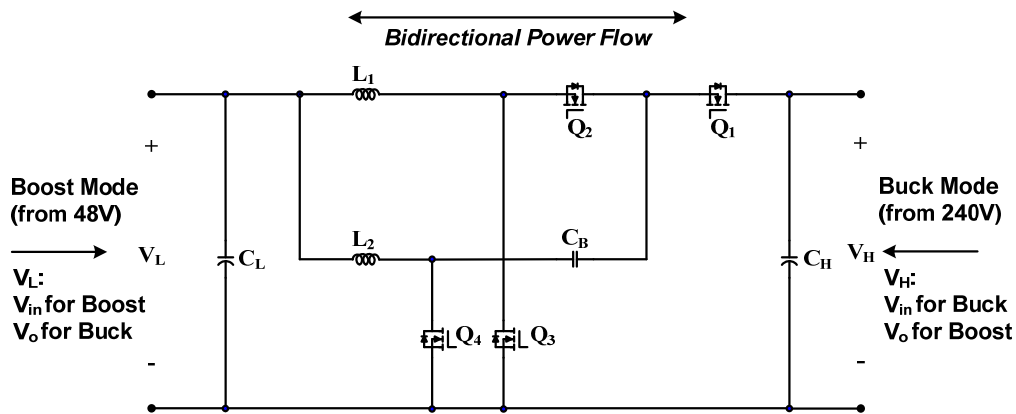


Figure 2. Proposed two-phase interleaved bidirectional DC/DC converter topology.

2.1. Charge Mode Operation

Figures 3 and 4 show the circuit configuration and typical waveforms of the proposed bidirectional converter in charge mode operation, respectively. It can be seen that switches Q_1 and Q_2 are driven with the phase-shift angle of 180° ; Q_3 and Q_4 work as synchronous rectification. Referring to typical waveforms shown in Figure 4, when the duty ratio is lower than 0.5, there are four operation modes as shown in Figure 5 according to the ON/OFF status of the active switches, and the operating principle of the proposed converter in charge mode operation can be explained briefly as follows:

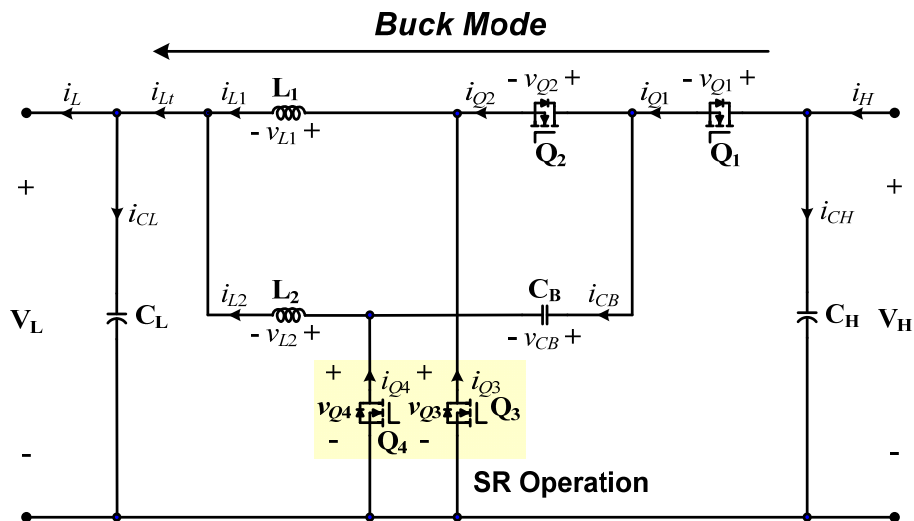


Figure 3. Circuit configuration of the proposed converter in the charge mode operation.

Mode 1 [t_0-t_1]: The interval time is DdT_{sw} , in this mode, switches Q_1 , Q_3 turned on and switches Q_2 , Q_4 are all off. The voltage across L_1 is the negative low-side voltage V_L , and hence i_{L1} decreases linearly from the initial value. Also, the voltage across L_2 is the difference of the high-side voltage V_H , the charge-pump voltage V_{CB} , and the low-side voltage V_L , and its level is positive. The voltages across inductances L_1 and L_2 can be represented as follows:

$$L_1 \frac{di_{L1}}{dt} = -V_L \tag{1}$$

$$L_2 \frac{di_{L2}}{dt} = V_H - V_{CB} - V_L \tag{2}$$

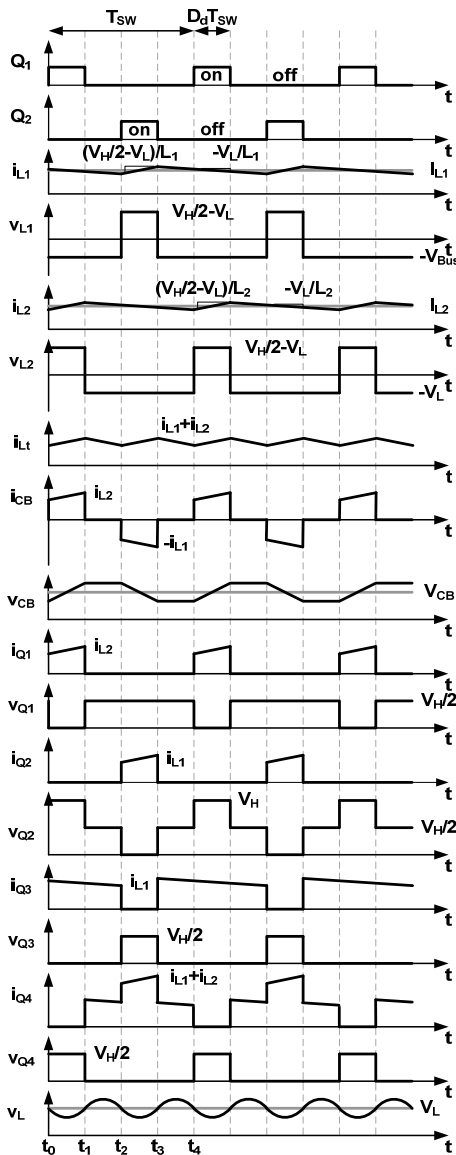


Figure 4. Typical waveforms of the proposed converter in the charge mode operation.

Mode 2 [t₁–t₂]: For this mode, the interval time is (0.5 – D_d) T_{sw}, switches Q₃, Q₄ are turned on and switches Q₁, Q₂ are all off. Both voltages across inductors L₁ and L₂ are the negative the low-side voltage V_L, hence i_{L1} and i_{L2} decrease linearly. The voltages across inductances L₁ and L₂ can be represented as follows:

$$L_1 \frac{di_{L1}}{dt} = L_2 \frac{di_{L2}}{dt} = -V_L \tag{3}$$

Mode 3 [t_2-t_3]: For this mode, the interval time is $D_d T_{sw}$, switches Q_2, Q_4 are turned on and switches Q_1 and Q_3 are all off. The voltage across L_1 is the difference between the charge-pump voltage V_{CB} with the low-side voltage V_L , and L_2 is keeping the negative low-side voltage V_L . The voltages across inductances L_1 and L_2 can be represented as follows; additionally, in steady state, the charge-pump voltage V_{CB} is equal to $V_H/2$:

$$L_1 \frac{di_{L1}}{dt} = V_{CB} - V_L \tag{4}$$

$$L_2 \frac{di_{L2}}{dt} = -V_L \tag{5}$$

Mode 4 [t_3-t_4]: From this operation mode, the interval time is $(0.5 - D_d) T_{sw}$. Switches Q_3, Q_4 are turned on and switches Q_1, Q_2 are all off, and its operation is the same with that of mode 2.

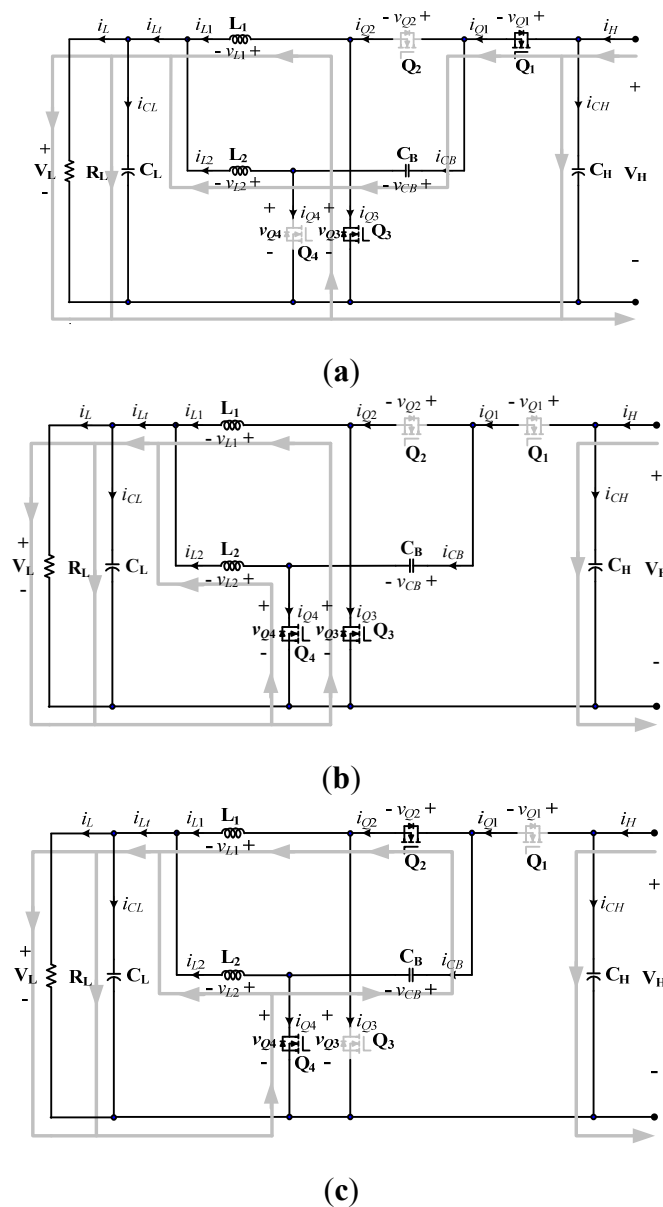


Figure 5. Operating modes of the proposed converter in the charge mode operation. (a) Mode 1; (b) Mode 2 and Mode 4; and (c) Mode 3.

2.2. Discharge Mode Operation

Figures 6 and 7 show the circuit configuration and typical waveforms of the proposed bidirectional converter in discharge mode operation, respectively. It can be seen that switches Q_3, Q_4 are driven with the phase-shift angle of 180° ; Q_1, Q_2 are used for the synchronous rectifier. Referring to typical waveforms shown in Figure 7, when the duty ratio is larger than 0.5, there are four operation modes as shown in Figure 8 according to the ON/OFF status of the active switches, and the operating principle of the proposed converter in discharge mode operation can be explained briefly as follows.

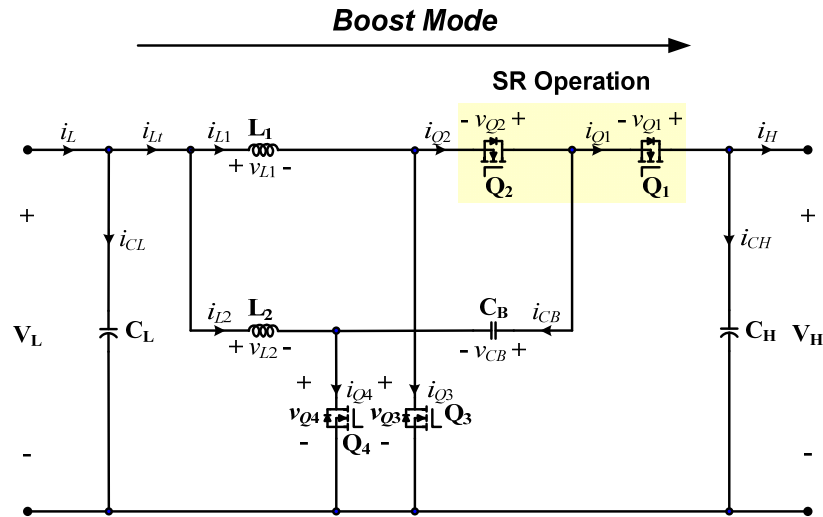


Figure 6. Circuit configuration of the proposed converter in the discharge mode operation.

Mode 1 $[t_0-t_1]$: The interval time is $(D_b - 0.5) T_{sw}$, switches Q_3 and Q_4 are turned on; switches Q_1 and Q_2 are all off. The low-side voltage V_L stays between inductance L_1 and L_2 , making the inductance current increase linearly, and begins to deposit energy. The voltages across inductances L_1 and L_2 can be represented as Equation (6).

$$L_1 \frac{di_{L1}}{dt} = L_2 \frac{di_{L2}}{dt} = V_L \tag{6}$$

Mode 2 $[t_1-t_2]$: For this operation mode, the interval time is $(1 - D_b) T_{sw}$. Switch Q_1, Q_3 remains conducting and Q_2, Q_4 are turned off. The voltages across inductances L_1 and L_2 can be represented as following equations:

$$L_1 \frac{di_{L1}}{dt} = V_L \tag{7}$$

$$L_2 \frac{di_{L2}}{dt} = V_L + V_{CB} - V_H \tag{8}$$

Mode 3 $[t_2-t_3]$: In this mode, both Q_3 and Q_4 are turned on, switches Q_1 and Q_2 are all off; the circuit operation is same as mode 1.

Mode 4 $[t_3-t_4]$: During this mode, the interval time is $(1 - D_b) T_{sw}$. For the low-side stage, switches Q_1, Q_3 are turned off and Q_2, Q_4 are turned on. The energy stored in inductor L_1 is now released energy to charge-pump capacitor C_B for compensating the lost charges in previous modes. Furthermore,

the output power is supplied from the capacitor C_H . The voltages across inductances L_1 and L_2 can be represented as follows:

$$L_1 \frac{di_{L1}}{dt} = V_L - V_{CB} \tag{9}$$

$$L_2 \frac{di_{L2}}{dt} = V_L \tag{10}$$

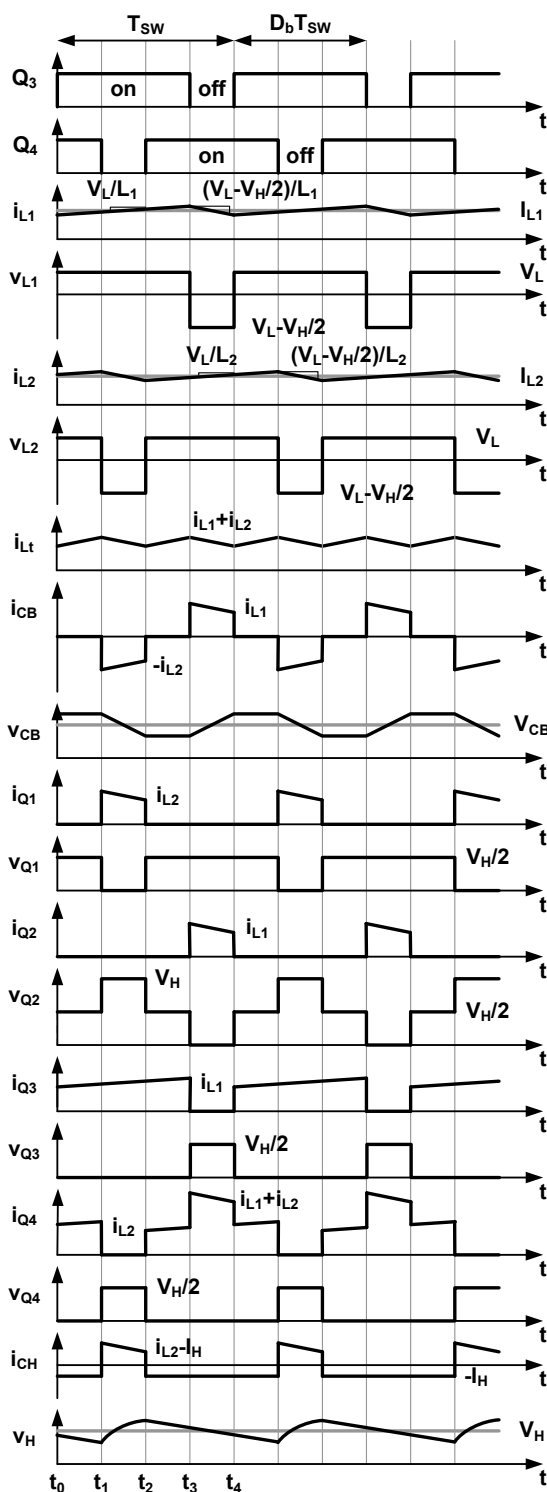


Figure 7. Typical waveforms of the proposed converter in the discharge mode operation.

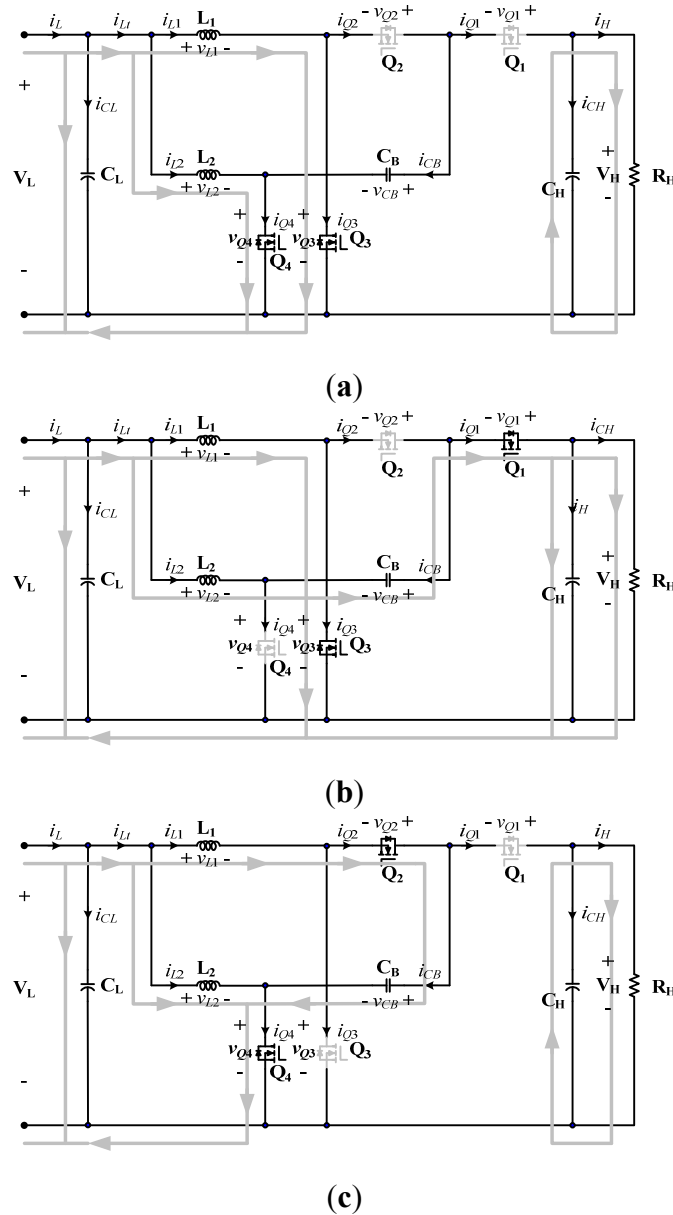


Figure 8. Operating modes of the proposed converter in the discharge mode operation. (a) Mode 1 and Mode 3; (b) Mode 2; and (c) Mode 4.

3. Steady-State Analyses

3.1. Voltage Conversion Ratio

The energy of proposed bidirectional converter can flow in both directions; in charge mode, V_H is the input and V_L is the output. According to Equations (1)–(5) and based on the voltage-second balance principle in L_1 and L_2 , the voltage conversion ratio M_d in the charge mode can be derived as:

$$M_d = \frac{V_L}{V_H} = \frac{D_d}{2} \tag{11}$$

where D_d is the duty ratio of the active switches Q_1 and Q_2 . As can be seen, the voltage conversion ratio in charge mode of the proposed converter is half of that of the conventional buck converter.

Similarly, in discharge mode, V_L is the input and V_H is the output. According to Equations (6)–(10) and based on the voltage-second balance principle in L_1 and L_2 , the voltage conversion ratio M_b in the discharge mode can be derived as:

$$M_b = \frac{V_H}{V_L} = \frac{2}{1 - D_b} \tag{12}$$

where D_b is the duty ratio of the active switches Q_3 and Q_4 . As can be seen, the voltage conversion ratio in discharge mode of the proposed converter is twice of that of the conventional boost converter.

As an illustration, Figure 9 shows the ideal voltage conversion ratio characteristic as a function of duty ratio. As shown in Figure 9, in the case of $D_d < 0.5$, the proposed converter has a higher voltage step-down conversion ratio than the conventional buck converter; furthermore, in the case of $D_b > 0.5$, the proposed converter has a higher voltage step-up conversion ratio than the conventional boost converter. As a results the proposed converter can overcome the extremely short duty ratio, which appears in the conventional buck/boost bidirectional converter [14,21].

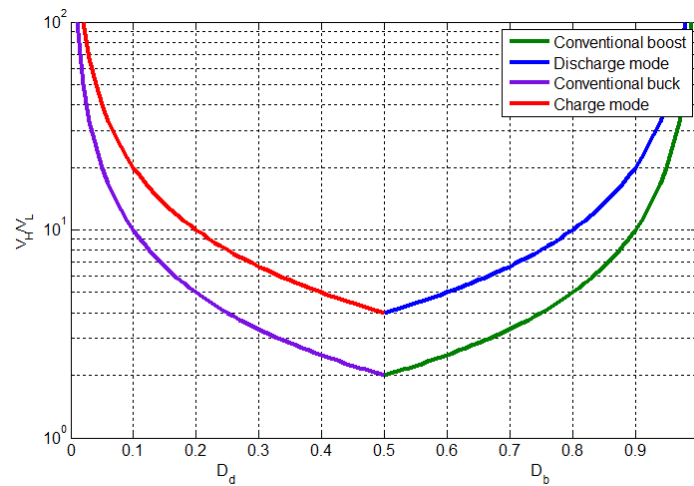


Figure 9. Voltage conversion ratio characteristic of the conventional buck, boost, and the proposed converter for charge and discharge operations respectively.

3.2. Switch Voltage Stress

Based on the aforementioned operation analyses, the open circuit voltage stress of switches $Q_1 \sim Q_4$ can be obtained directly as follows:

$$V_{Q1,max} = V_{Q3,max} = V_{Q4,max} = \frac{V_H}{2} \tag{13}$$

$$V_{Q2,max} = V_H \tag{14}$$

3.3. Inductor Current Ripple

According to Equations (1)–(5), the total ripple current of the inductor of the proposed converter in charge mode can be expressed as:

$$\Delta i_{L_t}|_{\text{charge}} = \frac{V_H T_{sw}}{L_s} (0.5 - D_d) D_d \tag{15}$$

Similarly, in discharge mode, according to Equations (6)–(10), the total ripple current of the inductor of the proposed converter in discharge mode can be expressed as:

$$\Delta i_{L_t}|_{\text{discharge}} = \frac{V_H T_{sw}}{L_s} (D_b - 0.5)(1 - D_b) \tag{16}$$

Figure 10 shows the normalized ripple current of the inductor of the proposed converter and the conventional buck/boost bidirectional converter for charge mode (*i.e.*, buck operation) and discharge mode (*i.e.*, boost operation), respectively. It can be mentioned that, in this figure, the inductor and the switching frequency of the two converters are equal. The ripple current of the conventional buck/boost bidirectional converter is normalized as one under duty ratio is equal to 0.5. It can be seen that from Figure 10, the maximum ripple current of the inductor of proposed converter is only half of that of conventional buck/boost bidirectional converter. On the other hand, if the ripple currents are equal, the inductor of the proposed converter is only half of that of conventional buck/boost bidirectional converter, which means that the proposed converter has a better dynamic response and smaller size.

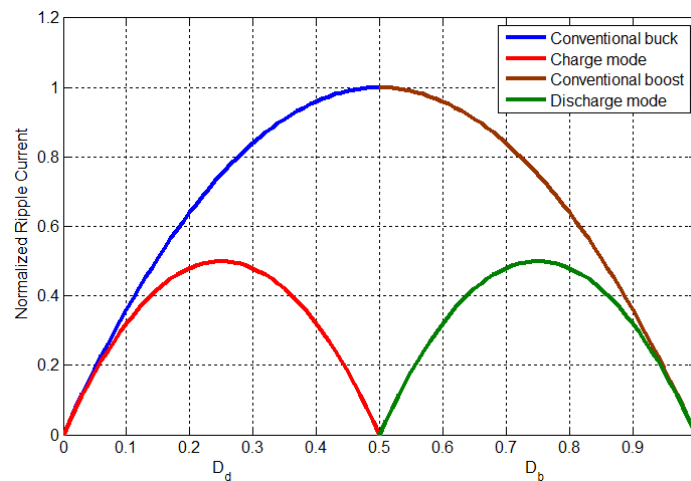


Figure 10. Normalized inductance ripple current *versus* duty ratio of the conventional buck, boost and the proposed converter for charge and discharge operations, respectively.

3.4. Boundary Conduction Mode Condition

The boundary normalized inductor time constant $\tau_{L,B}$ can be defined as follows:

$$\tau_{L,B} = \frac{L_s f_{sw}}{R} \tag{17}$$

During boundary conduction condition (BCM) operation, the output current of the proposed converter in charge mode can be derived as:

$$I_L = \frac{V_L}{L_s f_{sw}} (1 - D_d) \tag{18}$$

Substituting Equation (18) into Equation (17), the boundary normalized time constant in charge mode can be expressed as follows:

$$\tau_{Ld,B} = 1 - D_d \tag{19}$$

Similarly, in discharge mode, the output current of the proposed converter can be obtained as follows:

$$I_H = \frac{V_H}{4L_s f_{sw}} D_b (1 - D_b)^2 \tag{20}$$

The boundary normalized time constant in discharge mode can be expressed as follows:

$$\tau_{Lb,B} = \frac{D_b (1 - D_b)^2}{4} \tag{21}$$

Figure 11 shows the plots of boundary normalized inductor time constant curves $\tau_{Ld,B}$ and $\tau_{Lb,B}$ in charge and discharge modes. The proposed converter in the charge mode operates in CCM when τ_{Ld} is designed to be higher than the boundary curve of $\tau_{Ld,B}$. The proposed converter in the discharge mode operates in DCM when τ_{Lb} is selected to be lower than the boundary curve of $\tau_{Lb,B}$.

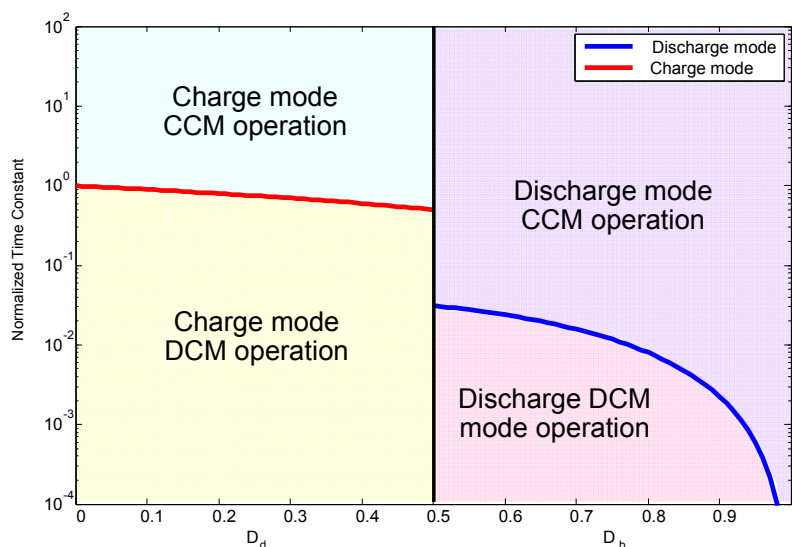


Figure 11. Normalized boundary inductances time constant in discharge and charge modes.

The proposed converter can operate not only in charge mode but also in discharge mode, the boundary inductance can be derived from Equations (18) and (20) as follows:

$$L_{d,B} = \frac{1 - D_d}{f_{sw}} \frac{V_L^2}{P_{out,d}} \tag{22}$$

$$L_{d,B} = \frac{1 - D_d}{f_{sw}} \frac{V_L^2}{P_{out,d}} \tag{23}$$

where $P_{out,d}$ and $P_{out,b}$ are the output power in charge and discharge modes, respectively.

Figure 12 shows the boundary inductances curve of the proposed converter in charge and discharge modes. If the inductance is selected to be larger than the boundary inductance, the proposed converter will operate in CCM. Experimental verifications of the proposed converter based on the steady-state

continuous conduction mode (CCM) are provided as Section 5. As to the discontinuous conduction mode (DCM) operation, the current stress is higher than that of CCM operation. In fact, the peak-to-peak input current ripple in DCM is so large as to reduce the life time of the battery stack due to the internal temperature rise, and the corresponding conversion efficiency of battery will be reduced as well [26]. Therefore, the operation of the converter in DCM is not suitable for battery applications, and only the CCM is discussed in this study.

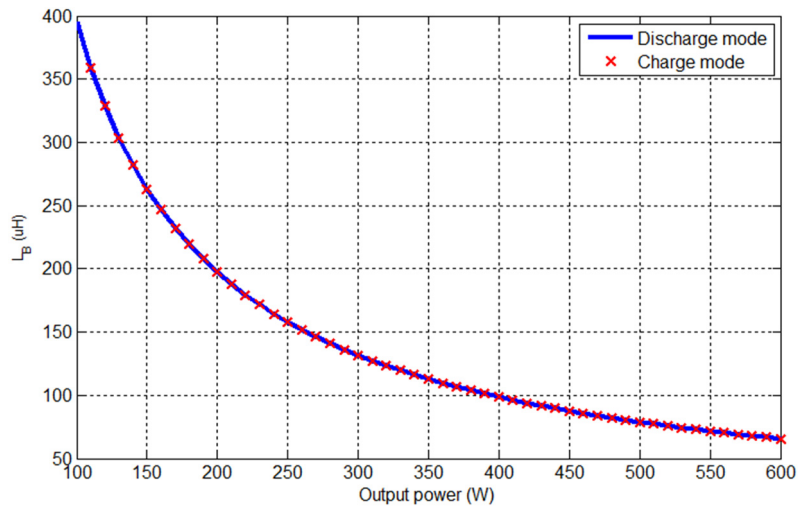


Figure 12. Boundary inductances in various power conditions.

4. Closed-Loop Control Strategy

As mentioned in previous sections, the proposed bidirectional converter is controlled by the specific duty ratio of switches $Q_1 \sim Q_4$. By proper regulation of duty ratio, the bidirectional voltage control can be adjustable. To design the closed-loop controller and simplify the mathematics for the converter, the PSIM circuit model is built under the following assumptions: (1) power switches and diodes are ideal; (2) equivalent series resistances of all inductors and capacitors of proposed converter are considered to obtain a relatively precise dynamic model; (3) converter is operated under CCM. In the PSIM circuit model, the adopted circuit parameters are $L_1 = L_2 = 250 \mu\text{H}$, $C_B = 10 \mu\text{F}$, $C_H = C_L = 440 \mu\text{F}$, output resistance in charge mode $R_L = 4.6 \Omega$, output resistance in discharge mode $R_H = 115.2 \Omega$, and equivalent series capacitances $r_{CB} = r_{CH} = r_{CL} = 10 \text{ m}\Omega$.

Figure 13 shows the block diagram of developed closed-loop control scheme for the proposed bidirectional converter. It can be seen that instead of controlling the output voltage of each module, the output voltage is sensed and compared with the reference voltage. The output voltage controller generates the total inductor current reference for the whole system, and the equal current-sharing between the two interleaved phases can be also obtained.

In the inner current control loop as shown in Figure 13, F_M is the constant gain of the PWM generator; G_{id} is the transfer function from duty ratio to total inductor current; C_i represents the transfer function of current controllers, and H_i is the sensing gain of the current sensor.

In the outer voltage control loop, G_{vd} represents the transfer function from duty ratio to output voltage; C_v is the transfer function of output voltage controller; and H_v is the sensing gain of the voltage sensor.

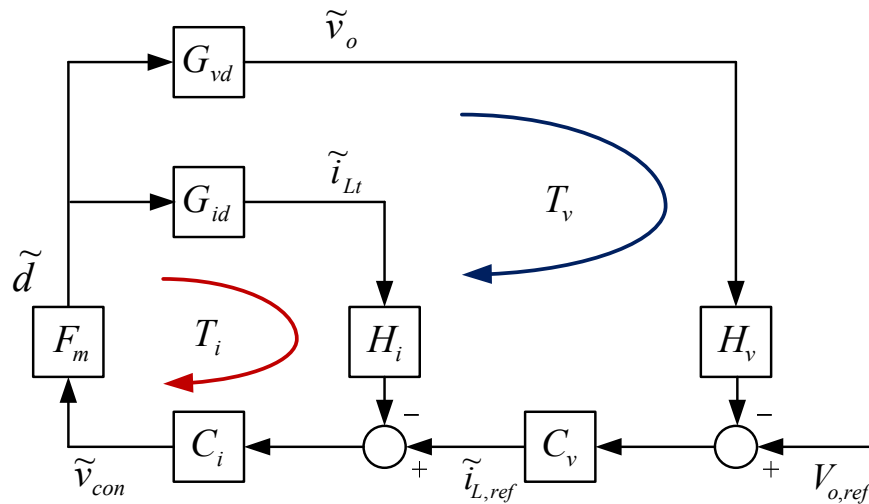


Figure 13. Block diagram of the closed-loop control scheme.

From Figure 13, open loop gain of the voltage loop and current loop of the converter can be derived as:

$$T_i = F_m G_{id} H_i C_i \tag{24}$$

$$T_v = \frac{G_{vd} H_v}{G_{id} H_i} \frac{T_i}{1 + T_i} C_v \tag{25}$$

where, $F_M = 1/100$, $H_i = H_v = 1$.

The small-signal transfer function from duty ratio to total inductor current G_{id} and the duty ratio to output voltage G_{vd} for charge mode (buck operation) and discharge mode (boost operation) can be represented as follows, respectively:

$$\left\{ \begin{aligned} G_{id} &= \frac{V_H}{2R_L} \frac{R_L C_L s + 1}{C_L (L_1 // L_2) s^2 + \frac{L_1 // L_2}{R_L} s + 1} \\ G_{vd} &= \frac{V_H}{2} \frac{1}{C_L (L_1 // L_2) s^2 + \frac{L_1 // L_2}{R_L} s + 1} \end{aligned} \right. \quad \text{(Charge Mode)} \tag{26}$$

$$\left\{ \begin{aligned} G_{id} &= \frac{8V_H}{(1-D_b)^2 R_H} \frac{\frac{R_H C_H}{2} s + 1}{\frac{4C_H (L_1 // L_2)}{(1-D_b)^2} s^2 + \frac{4(L_1 // L_2)}{(1-D_b)^2 R_H} s + 1} \\ G_{vd} &= \frac{V_H}{(1-D_b)} \frac{1 - \frac{(L_1 // L_2)}{(1-D_b)^2 R_H} s}{\frac{4C_H (L_1 // L_2)}{(1-D_b)^2} s^2 + \frac{4(L_1 // L_2)}{(1-D_b)^2 R_H} s + 1} \end{aligned} \right. \quad \text{(Discharge Mode)} \tag{27}$$

As above-mentioned, transfer functions in charge and discharge modes of the proposed bidirectional converter are different, consequently, for each mode, different controller is needed to be designed separately. In order to provide sufficient DC gain, bandwidth, gain/phase margins for the system, a simple type-II controller that include one-zero, one-pole, and another one-pole at the origin is used for the current loop

compensation. Furthermore, a PI controller that include one-zero and one-pole at origin is adopted for the voltage loop compensation.

The corresponding current/voltage controllers of the proposed converter for charge mode (buck operation) and discharge mode (boost operation) are selected as follows, respectively:

$$\begin{cases} C_i = 25000 \cdot \frac{s + 2000}{s(s + 20000)} \\ C_v = \frac{s + 1000}{s} \end{cases} \quad \text{(Charge Mode)} \quad (28)$$

$$\begin{cases} C_i = 20000 \cdot \frac{s + 2000}{s(s + 20000)} \\ C_v = 4 \cdot \frac{s + 200}{s} \end{cases} \quad \text{(Discharge Mode)} \quad (29)$$

Figure 14a illustrates the loop gain frequency response of compensated current loop in discharge mode operation, under full-load condition. As can be seen, this design results in a phase margin of 53 degree and the crossover frequency is about 1.5 kHz. Figure 14b illustrates the loop gain frequency response of compensated voltage loop in discharge mode operation, under full-load condition. This design results in a phase margin of 77 degree and the crossover frequency is about 327 Hz.

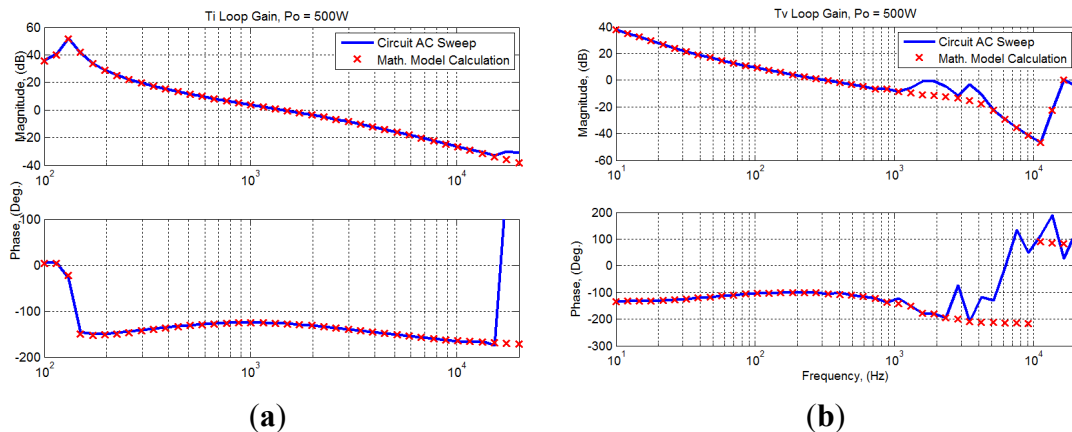


Figure 14. Loop gain frequency responses of compensated in discharge mode operation (a) current loop and (b) voltage loop.

Figure 15a illustrates the loop gain frequency response of the compensated current loop in charge mode operation, under a full-load condition. As can be seen, this design results in a phase margin of 51 degrees and the crossover frequency is about 1.8 kHz. Figure 15b illustrates the loop gain frequency response of compensated voltage loop in charge mode operation, under both full-load condition. This design results in a phase margin of 81.7 degree and the crossover frequency is about 282 Hz.

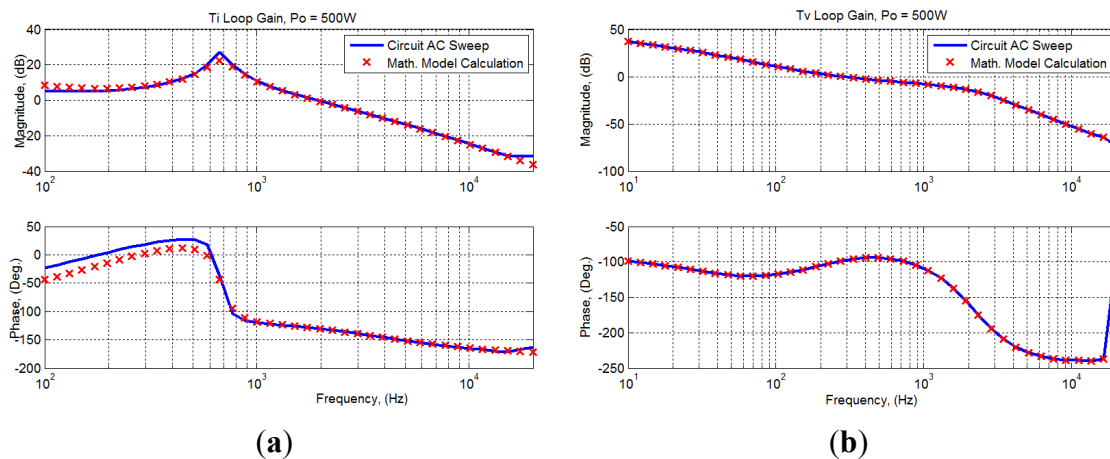


Figure 15. Loop gain frequency responses of compensated in charge mode operation (a) current loop and (b) voltage loop.

5. Simulation and Experimental Results

To facilitate understanding the merits and serve as a verification of the effectiveness of the proposed converter, a 500 W prototype system, its PSIM simulations and experimental results are constructed. All the experimental waveforms are measured by a digital phosphor oscilloscope, MDO-3024 with DC variable gain accuracy of $\pm 3.0\%$ [27]. As the low-side power source, the vehicle battery bank consists of four 12 V lead-acid batteries in series connection, and battery string voltage is around 44 V~53 V (nominal voltage: 48 V). The high-side DC-bus voltage of the DC-microgrid system is to keep around 216 V~264 V (nominal voltage: 240 V). The switching frequency of the prototype circuit is 35 kHz and the corresponding component parameters are listed in Table 1 for reference.

Table 1. Component parameters of the prototype.

Components	Symbol	Value/Part No.
Two-Phase inductors	L_1, L_2	250 μ H
Power switches	$Q_1 \sim Q_4$	W45NM60
Charge-pump capacitor	C_B	10 μ F/250 V
High-side capacitor	C_H	440 μ F/500 V
Low-side capacitor	C_L	440 μ F/500 V

To check the validity of Equations (11) and (13)–(15) in charge mode operation, both simulation and experimental results are recorded as shown in Figures 13–15. From Figures 16–18, one can see that, with the proposed converter, the nearly 48 V low-side output voltage can be achieved easily with a rather low duty ratio of 0.4. Similarly, to check the validity of Equations (12)–(14) and (16) in discharge mode operation, both simulation and experimental results are recorded as shown in Figures 19–21. From Figures 19–21, one can see that, with the proposed converter, the nearly 240 V high-side output voltage can be achieved easily with a rather low duty ratio of 0.6.

From these figures in charge and discharge operations, one can observe that the charge-pump capacitor indeed can share half of the high-side voltage for reducing the voltage stress of the almost active switches ($Q_1, Q_3,$ and Q_4), which are also very close to that calculated from Equations (13) and (14). Obviously,

the voltage stress of the almost active switch is much smaller than the high-side voltage and enables one to adopt lower voltage rating device for reducing the conduction loss as well as switching loss. Furthermore, due to the lower duty ratio, not only can the output voltage regulation range be further extended but the resulting conduction loss can also be further reduced due to the shorter conduction period. Furthermore, from Figures 17 and 20, the two-phase interleaving operation of the proposed converter can be achieved effectively, partially cancel the output and input ripples for charge and discharge operations, respectively.

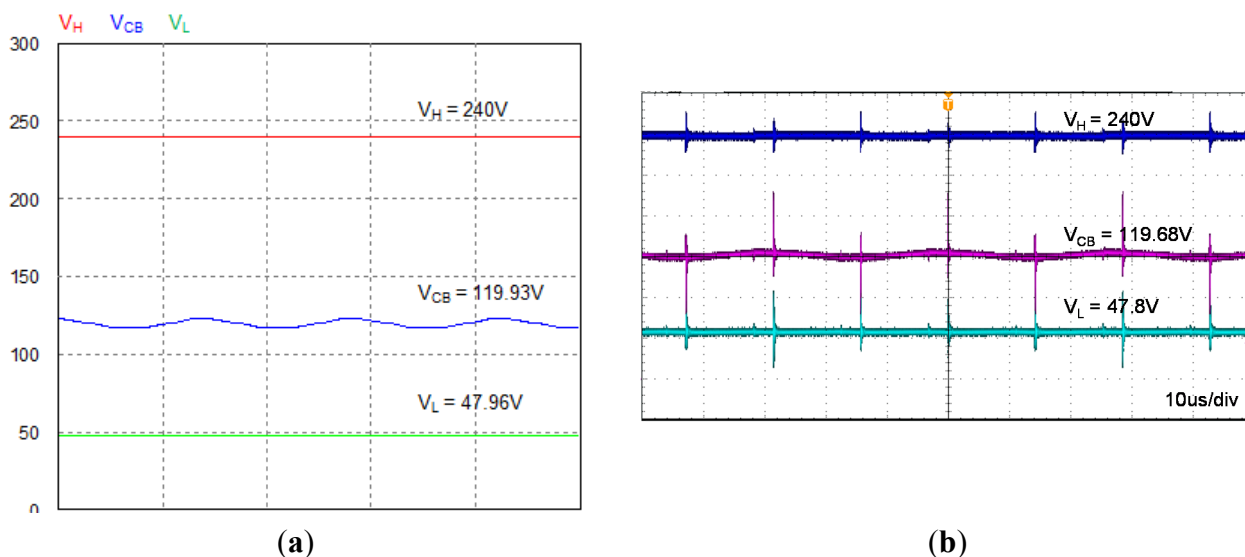


Figure 16. Waveforms of input voltage, output voltage and charge-pump capacitor voltage in the charge mode at full load (a) by simulation; and (b) by measurement.

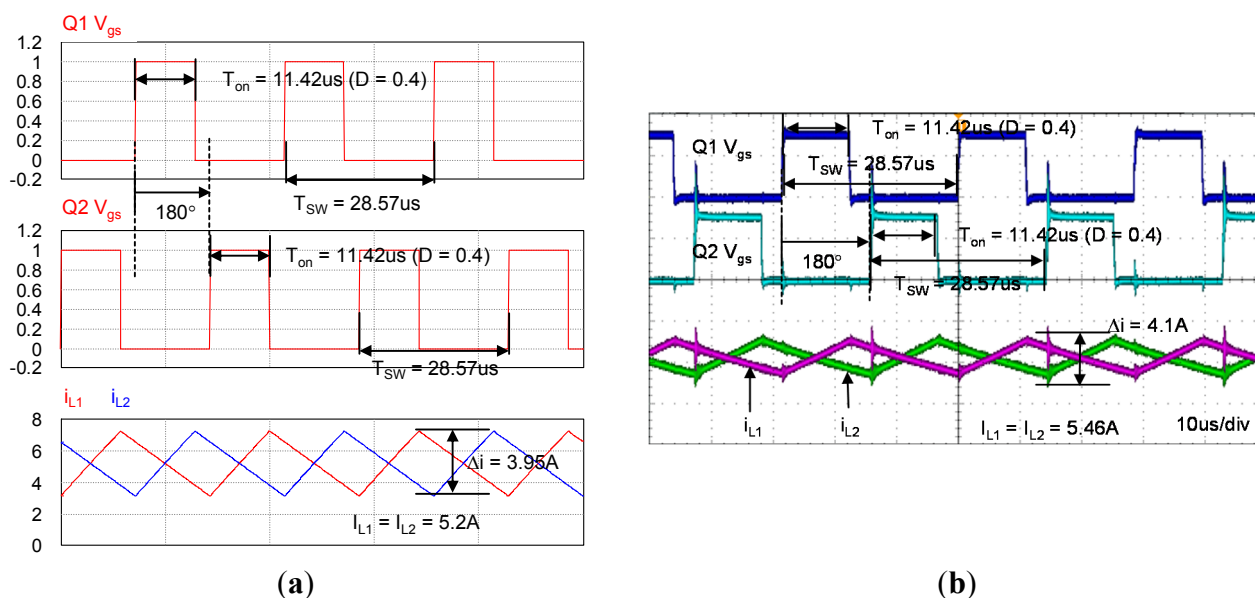


Figure 17. Waveforms of gate signals of high-side switches $Q_1\sim Q_2$, and two-phase inductor currents $i_{L1}\sim i_{L2}$ in the charge mode at full load (a) by simulation; and (b) by measurement.

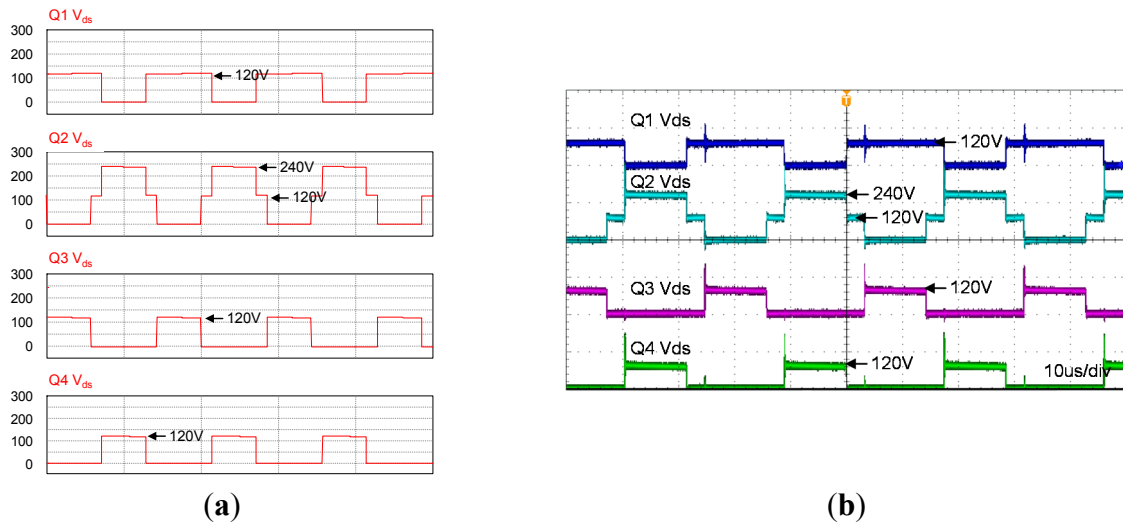


Figure 18. Waveforms of open-circuit voltage of switches $Q_1\sim Q_4$ in the charge mode at full load (a) by simulation; and (b) by measurement.

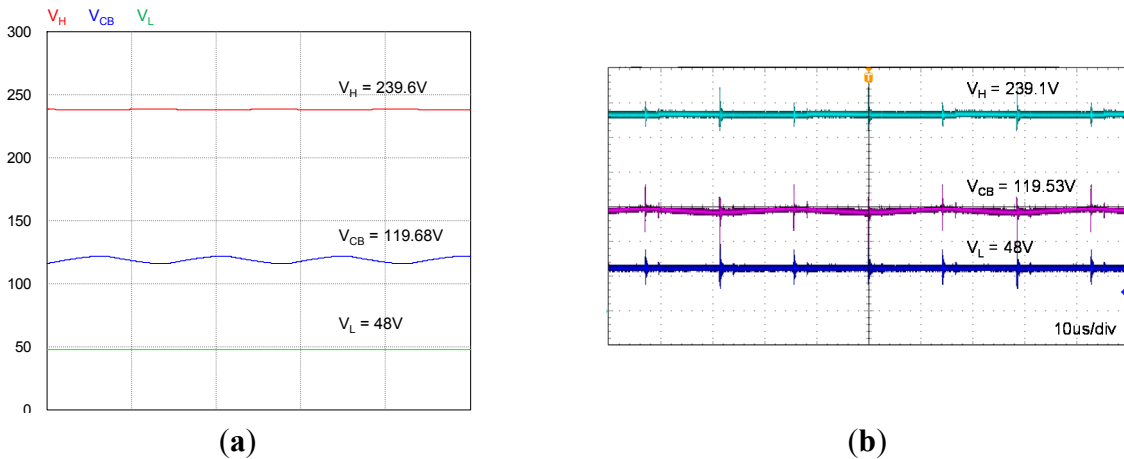


Figure 19. Waveforms of input voltage, output voltage and charge-pump capacitor voltage in the discharge mode at full load (a) by simulation; and (b) by measurement.

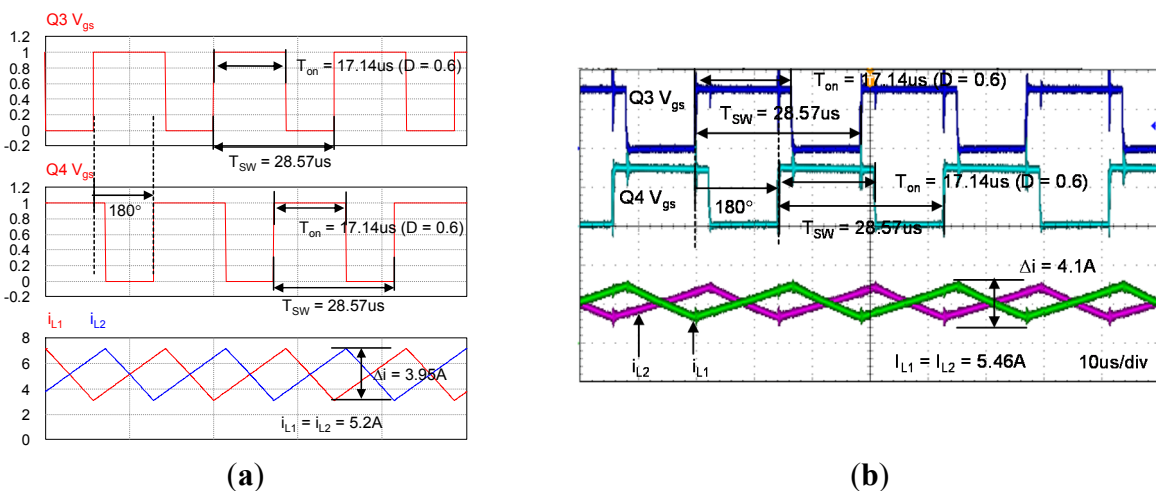


Figure 20. Waveforms of gate signals of low-side switches $Q_3\sim Q_4$, and two-phase inductor currents $i_{L1}\sim i_{L2}$ in the discharge mode at full load (a) by simulation; and (b) by measurement.

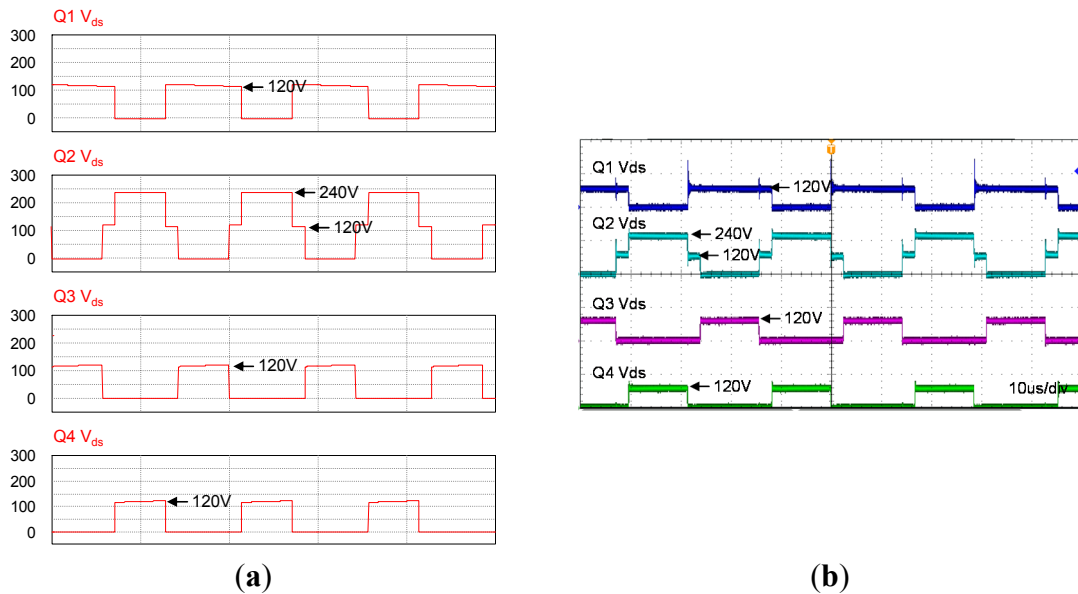


Figure 21. Waveforms of open-circuit voltage of switches Q_1 – Q_4 in the discharge mode at full load (a) by simulation; and (b) by measurement.

Figures 22 and 23 present the transient response due to a step load current change between 250 W–500 W for the prototype system. It is seen that from these figures, with the proposed closed-loop control scheme, the over-current problem under transient conditions can be prevented. Also, the converter bidirectional output voltages are well regulated at 48 V and 240 V in charge and discharge modes, respectively.

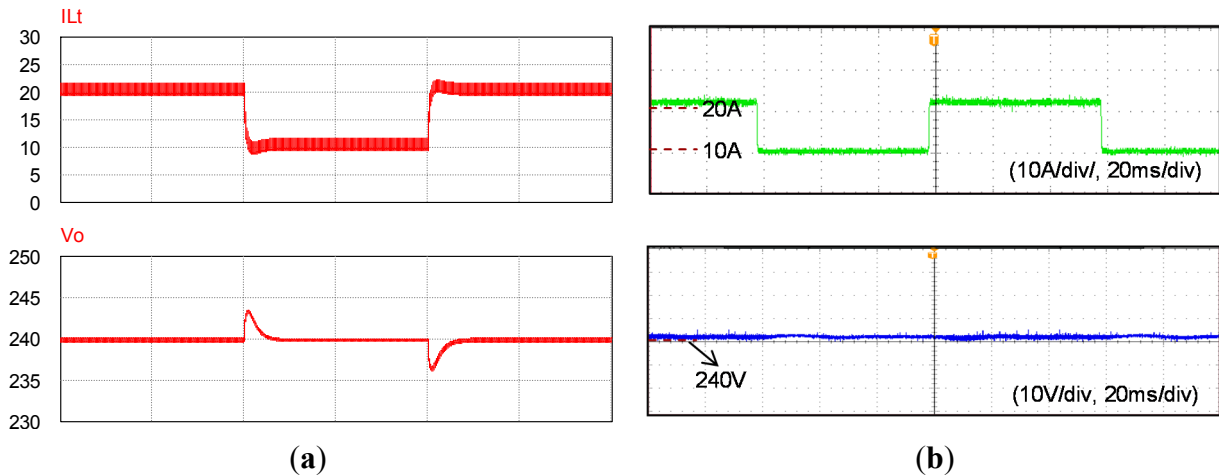


Figure 22. Waveforms of transient response for load period steps in discharge mode from 500 W to 250 W and then back to 500 W: (a) by simulation; and (b) by measurement.

Figure 24 shows the realized prototype of the proposed converter, and its conversion efficiency performance is measured by using a precision power analyzer, Yokogawa-WT3000, with the basic accuracy of 0.01% of reading [28] as shown in Figure 25. For the comparison, the measured efficiency in the conventional bidirectional buck/boost converter is also shown in Figure 25. It can be seen that, for the proposed converter is operated in charge mode, the maximum efficiency is 98.4%, and the efficiency at full load is 94.3%. Furthermore, for the proposed converter is operated in discharge mode, the maximum efficiency is 97.7%, and the efficiency at full load is 94.9%. Also, the measured efficiency

of the conventional bidirectional buck/boost converter is around 81.5%–92.2% in discharge mode and is around 82.5%–93.2% in charge mode. It is seen from Figure 25 that the measured efficiency of the proposed converter are higher than the conventional bidirectional buck/boost converter.

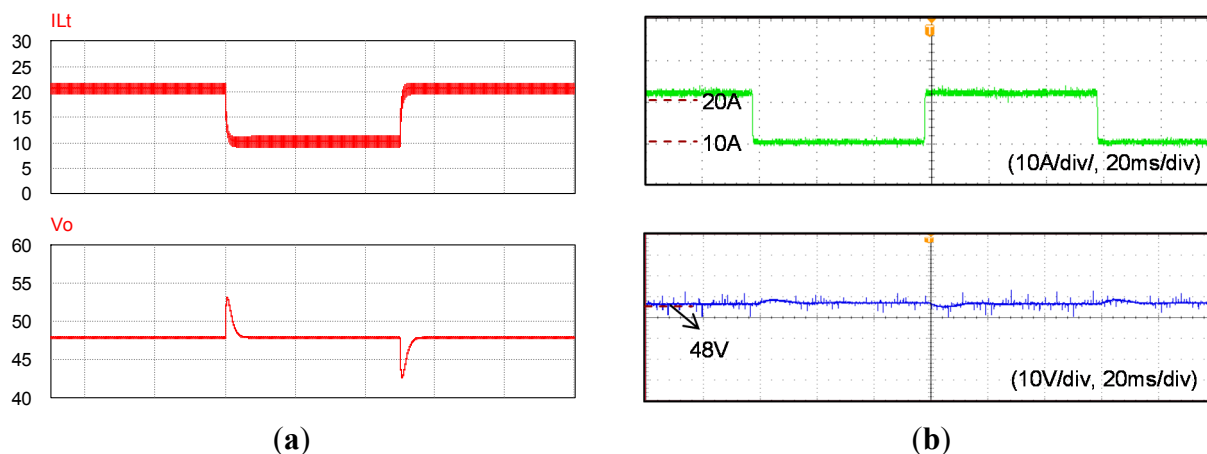


Figure 23. Waveforms of transient response for load period steps in charge mode from 500 W to 250 W and then back to 500 W: (a) by simulation; and (b) by measurement.

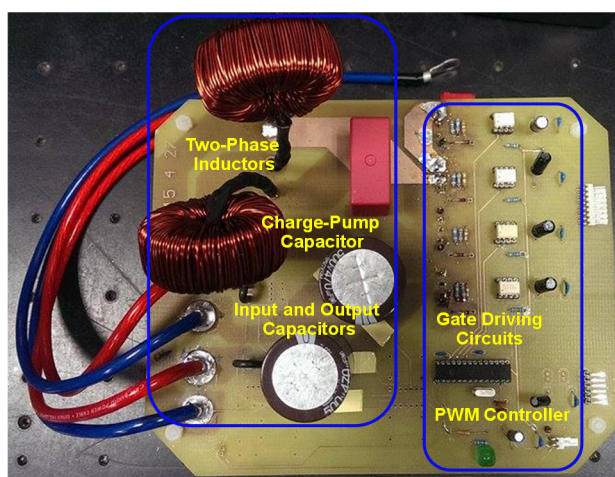


Figure 24. Realized prototype of the proposed converter.

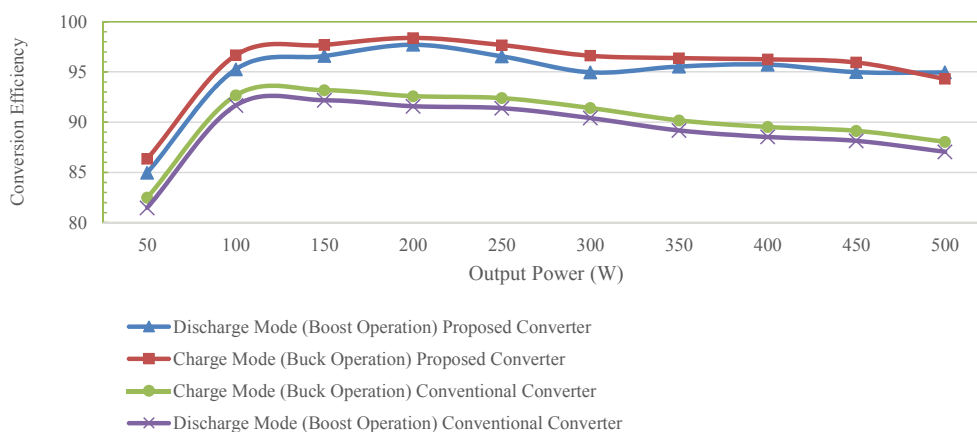


Figure 25. Measured efficiency in the proposed converter and conventional bidirectional buck/boost converter.

The performance comparisons of the proposed bidirectional converter with a variety of research in the announced works are summarized in Table 2. It can be seen that the amounts of passive components in [23,24] are more than the requirement in the proposed converter. It will result in the increase of manufacturing cost. Additionally, the voltage conversion ratio of the previous bidirectional converter in [25] is the same as the proposed one in this study. Thanks to adding only one charge-pump capacitor, the proposed two-phase interleaved bidirectional converter indeed performs the higher conversion efficiency, bidirectional power flow, lower output current, and voltage ripples under 500 W power rating with the better price-performance ratio than other announced works [23–25].

Table 2. Characteristic comparison among a variety of converters.

Items	Topology			
	[23]	[24]	[25]	Proposed
Switching control structure	single-phase	single-phase	single-phase	two-phase
Output ripple	High	High	Medium	Low
Number of main switches	4	4	4	4
Passive components	6	6	4	5
Step-up conversion ratio	$(n^* + 2)/D_b$	$n/(1 - D_b)$	$2/(1 - D_b)$	$2/(1 - D_b)$
Step-down conversion ratio	$D_d/(n + 2)$	$D_d/(1 + n - nD_d)$	$D_d/2$	$D_d/2$
High-side voltage	200 V	200 V	200 V	240 V
Low-side voltage	24 V	24 V	24 V	48 V
Realized prototype power rating	800 W	200 W	200 W	500 W
Maximum efficiency (step-down)	95.1%	91.6%	94.8%	98.4%
Maximum efficiency (step-up)	95.3%	94.3%	94.1%	97.7%

* n : the turns ratio of coupled inductors [23,24].

6. Conclusions

A bidirectional DC/DC converter topology is presented suitable for vehicle and DC-microgrid system application. Compared with the conventional buck/boost bidirectional converter, key features such as the improved voltage conversion ratio, lower switch voltage stress, lower current ripple and avoid operating at extreme duty ratios can be obtained by the studied converter. A 500 W laboratory prototype with bidirectional power flow capability are constructed to verify the feasibility, all experimental waveforms are closed to the theoretical analysis and simulation results. The maximum efficiency levels in discharge and charge modes are about 97.7% and 98.4%, respectively. Finally, it is worth mentioning that the proposed bidirectional converter configuration can be easily extended to more phases for higher power applications.

Acknowledgments

This research is partially sponsored by the Ministry of Science and Technology, Taiwan, under contracts MOST 104-2623-E-027-005-ET, and MOST 104-2221-E-027-125. It is also sponsored by the Ministry of Education, Taiwan, under NTUT Technological University Paradigms. The authors would like to express their appreciation to Yun-Hsiu Lee (NTUT) for the experimental bench setup.

Author Contributions

Ching-Ming Lai designed the study and performed experimentation process; all authors collected and analyzed data together; Ching-Ming Lai and Yuan-Chih Lin wrote the manuscript; Ching-Ming Lai and Dasheng Lee gave technical support and conceptual advice.

Conflicts of Interest

The authors declare no conflict of interest.

References

1. Carrasco, J.M.; Franquelo, L.G.; Bialasiewicz, J.T.; Galvan, E.; Guisado, R.C.P.; Prats, M.A.M.; Leon, J.I.; Moreno-Alfonso, N. Power-Electronic systems for the grid integration of renewable energy sources: A survey. *IEEE Trans. Ind. Electron.* **2006**, *53*, 1002–1016.
2. Vilathgamuwa, D.M.; Gajanayake, C.J.; Loh, P.C. Modulation and control of three-phase paralleled Z-source inverters for distributed generation applications. *IEEE Trans. Energy Convers.* **2009**, *24*, 173–183.
3. Guerrero, J.M.; Blaabjerg, F.; Zhelev, T.; Hemmes, K.; Monmasson, E.; Jemei, S.; Comech, M.P.; Granadino, R.; Frau, J.I. Distributed generation: Toward a new energy paradigm. *IEEE Ind. Electron. Mag.* **2010**, *4*, 52–64.
4. Pan, C.T.; Lai, C.M.; Cheng, M.C. A novel integrated single-phase inverter with auxiliary step-up circuit for low-voltage alternative energy source applications. *IEEE Trans. Power Electron.* **2010**, *25*, 2234–2241.
5. Gajanayake, C.J.; Vilathgamuwa, D.M.; Loh, P.C.; Teodorescu, R.; Blaabjerg, F. Z-Source-Inverter-Based flexible distributed generation system solution for grid power quality improvement. *IEEE Trans. Energy Convers.* **2009**, *24*, 695–704.
6. Infield, D.G.; Onions, P.; Simmons, A.D.; Smith, G.A. Power quality from multiple grid-connected single-phase inverters. *IEEE Trans. Power Deliv.* **2004**, *19*, 1983–1989.
7. Cheng, P.T.; Hou, C.C.; Huang, Y.F. Overload prevention. *IEEE Ind. Appl. Mag.* **2004**, *10*, 26–34.
8. Ueda, Y.; Kurokawa, K.; Tanabe, T.; Kitamura, K.; Sugihara, H. Analysis results of output power loss due to the grid voltage rise in grid-connected photovoltaic power generation systems. *IEEE Trans. Ind. Electron.* **2008**, *55*, 2744–2751.
9. Hatziargyriou, N.; Asano, H.; Iravani, R.; Marnay, C. Microgrids. *IEEE Power Energy Mag.* **2007**, *5*, 78–94.
10. Lai, C.M.; Pan, C.T.; Cheng, M.C. High-Efficiency modular high step-up interleaved boost converter for dc-microgrid applications. *IEEE Trans. Ind. Appl.* **2012**, *48*, 161–171.
11. Chukwu, U.C.; Mahajan, S.M. Real-Time management of power systems with V2G facility for smart-grid applications. *IEEE Trans. Sustain. Energy* **2014**, *5*, 558–566.
12. Yilmaz, M.; Krein, P.T. Review of the impact of vehicle-to-grid technologies on distribution systems and utility interfaces. *IEEE Trans. Power Electron.* **2013**, *28*, 5673–5689.
13. Mohan, N.; Undeland, T.M.; Robbins, W.P. *Power Electronics: Converters, Applications and Design*, 3rd ed.; Wiley: Hoboken, NJ, USA, 2003.

14. Chen, L.R.; Chu, N.Y.; Wang, C.S.; Liang, R.H. Design of a reflex-based bidirectional converter with the energy recovery function. *IEEE Trans. Ind. Electron.* **2008**, *55*, 3022–3029.
15. Chen, G.; Lee, Y.S.; Hui, S.Y.; Xu, D.; Wang, Y. Actively clamped bidirectional flyback converter. *IEEE Trans. Ind. Electron.* **2000**, *47*, 770–779.
16. Peng, F.Z.; Li, H.; Su, G.J.; Lawler, J.S. A new ZVS bidirectional dc-dc converter for fuel cell and battery application. *IEEE Trans. Power Electron.* **2004**, *19*, 54–65.
17. Yamamoto, K.; Hiraki, E.; Tanaka, T.; Nakaoka, M.; Mishima, T. Bidirectional DC-DC converter with full-bridge/push-pull circuit for automobile electric power systems. In Proceedings of the IEEE Power Electronics Specialists Conference, Jeju, Korea, 18–22 June 2006; pp. 1–5.
18. Jeong, G.Y. High efficiency asymmetrical half-bridge flyback converter using a new voltage-driven synchronous rectifier. *IET Power Electron.* **2010**, *3*, 18–32.
19. Hu, Y.; Xiao, W.; Li, W.; He, X. Three-Phase interleaved high-step-up converter with coupled-inductor-based voltage quadrupler. *IET Power Electron.* **2014**, *7*, 1841–1849.
20. Hu, Y.; Cao, W.; Finney, S.J.; Xiao, W.; Zhang, F.; McLoone, S.F. New Modular Structure DC-DC Converter without Electrolytic Capacitors for Renewable Energy Applications. *IEEE Trans. Sustain. Energy* **2014**, *5*, 1184–1192.
21. Jin, K.; Yang, M.; Ruan, X.; Xu, M. Three-Level bidirectional converter for fuel-cell/battery hybrid power system. *IEEE Trans. Ind. Electron.* **2010**, *57*, 1976–1986.
22. Yang, L.S.; Liang, T.J. Analysis and implementation of a novel bidirectional DC-DC converter. *IEEE Trans. Ind. Electron.* **2012**, *59*, 422–434.
23. Duan, R.Y.; Lee, J.D. High-Efficiency bidirectional DC-DC converter with coupled inductor. *IET Power Electron.* **2012**, *5*, 115–123.
24. Lin, C.C.; Yang, L.S.; Wu, G.W. Study of a non-isolated bidirectional DC-DC converter. *IET Power Electron.* **2013**, *6*, 30–37.
25. Liang, T.J.; Liang, H.H.; Chen, S.M.; Chen, J.F.; Yang, L.S. Analysis, design, and implementation of a bidirectional double-boost DC-DC converter. *IEEE Trans. Ind. Appl.* **2014**, *50*, 3955–3962.
26. Wen, H.; Xiao, W.; Wen, X.; Armstrong, P. Analysis and evaluation of DC-link capacitors for high-power-density electric vehicle drive systems. *IEEE Trans. Veh. Technol.* **2012**, 2950–2964. doi:10.1109/TVT.2012.2206082.
27. MDO3000 Oscilloscope Datasheet. Available online: <http://www.tek.com/datasheet/mdo3000/mdo3000-series-datasheet> (accessed on 3 May 2015).
28. WT3000E User's Manual. Available online: <http://tmi.yokogawa.com/products/digital-power-analyzers/digital-power-analyzers/precision-power-analyzer-wt3000e/> (accessed on 10 June 2015).